Geochemistry Geophysics Geosystems

Supporting Information for

Effect of melt/mantle interactions on MORB chemistry at the Easternmost Southwest Indian Ridge (61 to 67°E)

Marine Paquet[1], Mathilde Cannat[1], Daniele Brunelli[2,3], Cédric Hamelin[4], Eric Humler[5]

[1]Equipe de Géosciences Marines, Institut de Physique du Globe de Paris, Sorbonne Paris Cité, Université Paris Diderot, UMR7154 CNRS, 1, rue Jussieu, 75238 Paris cedex 05, France

[2]Dipartimento di Scienze Chimiche e Geologiche, Università di Modena e Reggio Emilia, Via Campi 103, 41125 Modena, Italy

[3]Institute for Marine Sciences, CNR – ISMAR, Bologna, Italy

[4]Centre for Geobiology, University of Bergen, Allegaten 41 5007, Bergen, Norway

[5]Laboratoire de Planétologie et Géodynamique, UMR 6112, CNRS, Université de Nantes, 2 rue de la Houssinière, 44322 Nantes, France

Contents of this file

Additional Supporting Information (Files uploaded separately)

Captions for Tables S1 to S8 (if larger than 1 page, upload as separate file)

Introduction

The supplementary materials include analytical methods used for this study, a description of the basalt dataset for the global mid-ocean ridge system, established using the PetDB database [*Lehnert et al.*, 2000]. We present the calculation parameters used for the mass balance model and the liquid lines of descent calculated with Petrolog [*Danyushevsky and Plechov*, 2011]. Additionally, the complete dataset for major element compositions of plagioclases, clinopyroxenes, orthopyroxenes, olivines and spinels analyzed in this study, as well as additional figures, are provided. We also present a list of all the ultramafic to gabbroic samples that were examined for this work, with their degrees of alteration and deformation.

Text S1.

1. Major elements

We measured in situ major element concentrations in basaltic fresh glasses, using the Cameca SX-100 electron microprobe (CAMPARIS service, Paris), under a 15kV tension and a 10nA beam current. The spot size was 10µm. Counting times for most measurements were 10s for Si, Al, K, Ca, Fe, Ti, Mn, Na, Mg and 20s for Cl, P and Ni. We also performed some measurements with 15kV, 20nA, 10µm, 30s for Na, Ti, Fe; 60s for Si, Ca, Mg, Al; 70s for K and 100s for Mn. Additional high-precision analyses of Cl were performed using a 15-kV tension, a 100-nA beam current and an integration of 10 points, 40s each, for every sample. Data presented here correspond to the mean values for each sample. We used the internal standard of the Lamont Doherty Laboratory, JDF-D2, to correct for instrumental deviations.

We also measured in situ major element concentrations in olivine, plagioclase, clinopyroxene, orthopyroxene and spinel, on 30 µm-thick polished thin sections, using the Cameca SX-100 electron microprobe (CAMPARIS service, Paris), under a 15kV tension and a 10nA beam current. The spot size was 0 µm. Counting times were 5s for Si, K, Fe, Na and 10s for Al, P, Ca, Cl, Cr, Mn, Ti, Ni, Mg and F. Additional high-precision analyses of Ni and Mn in olivine were performed using a 15kV tension, a 45nA beam current, and counting times of 20s for Ni, Mn, Cr and Ca.

2. Trace elements

In situ trace element compositions in basaltic samples were determined at Montpellier 2 University on a ThermoFinnigan Element 2 High Resolution-Inductively Coupled Plasma-Mass Spectrometer (HR-ICP-MS) using a single collector double-focusing sector field Element XR (eXtended Range) coupled with laser ablation (LA) system, a Geolas (Microlas) automated platform housing a 193 nm Compex 102 laser from LambdaPhysik.

Analyses were conducted using an in-house modified ablation cell of ca. 30 cm^3, which resulted in a shorter washout time and an improved sensitivity compared to the initial larger ablation cell. Ablation experiments were conducted in a helium atmosphere, which enhances sensitivity and reduces inter-element fractionation [*Gunther and Heinrich*, 1999]. The helium gas and particles from the sample were then mixed with argon before entering the plasma. Signals were acquired in Time Resolved Acquisition, devoting 2 min for the blank and 1 min for measurement of the analyses. The laser was fired using an energy density of 10 $J.cm^{-2}$ at a frequency of 5Hz. Basaltic glasses were measured using a spot size of 102 µm after pre-ablation at 122 µm. This resulted in an average sensitivity of more than 5000 cps/ppm up to 20,000 cps/ppm for most trace elements except for Ti, Ni and Zn (ca. 500 to 1000 cps/ppm) based on measurements on the NIST 612 certified reference material.

^{43}Ca was used as internal standard. Concentrations were calibrated against the NIST 612 rhyolitic glass using the values given in *Pearce et al.* [1997]. Data were subsequently reduced using the GLITTER software [*Van Achterberg et al.*, 2001] using the linear fit to ratio method. Oxide level, measured using the ThO/Th ratio, was below 0.7% yet, oxide interferences were detected on middle Rare Earth Elements and corrected using sample ED-DR26 as internal standard. Precision and accuracy, evaluated by repeated analyses of reference basalt BIR, were typically of <1 to 5% precision (1sigma) except for Pb, Rb and Ba (~ 9%), and

better than 15% accuracy for most analyses. Detection limits were between <1 and 50 ppb for most trace elements and ca. 500 ppb for Ti. The accuracy of the analyses is about <1 to 30% depending on the different trace elements.

In situ trace element compositions of clinopyroxene, orthopyroxene and plagioclase in the impregnated and reacted ultramafic rocks were measured at the CIGS (Centro Interdipartimentale Grandi Strumenti) in Modena University on a Thermo Fisher Scientific Quadrupole- Inductively Coupled Plasma-Mass Spectrometer (Q-ICP-MS) XSeries 2 coupled with laser ablation (LA) system UP213. Signals were acquired in Time Resolved Acquisition, devoting around 30s for the blank and 90s for measurement of the analyses. The laser was fired using an energy density of 25 $J.cm^{-2}$ at a frequency of 20Hz. Minerals were measured using a spot size of 80 µm after pre-ablation at 100µm. This resulted in an average sensitivity of more than 350 cps/ppm up to 3200 cps/ppm for most trace elements except for Ti, Ni and Zn (ca. 35 to 150 cps/ppm) based on measurements on the NIST 610, 612 and 614 certified reference material.

^{29}Si and ^{44}Ca were respectively used as internal standard for pyroxenes and plagioclase. Concentrations were calibrated against the NIST 610, 612 and 614 glasses using the values given in *Pearce et al.* [1997] and *Morishita et al.* [2005]. Data were subsequently reduced using the PlasmaLab software. Precision and accuracy, evaluated by repeated analyses of reference glasses NIST, were typically of 2 to 6% precision (1sigma) except for Th and U (~7-8%), and better than 15% accuracy for most analyses. The accuracy of the analyses is about <1 to 25-30% depending on the different trace elements.

3. Isotopes

Handpicked glass chips were washed for 10 minutes in 1% H_2O_2 in an ultrasonic bath, followed by three rinses in ultrapure water and then leached briefly in concentrated ultrapure HBr prior to digestion in concentrated HBr-HF ultrapure acids (1:3). Powders were leached in HCl 6M during one hour at 130°C, followed by three rinses in ultrapure water and drying. Lead was extracted after *Manhes et al.* [1978]. Nd separation was completed using a method adapted from *Hamelin et al.* [2013].

Nd and Pb isotopic compositions were measured at Institut de Physique du Globe de Paris using a Thermo-Scientific Neptune. All Nd data were corrected for mass fractionation using $^{146}Nd/^{144}Nd=0.7219$. Repeated measurements of NIST3135A and JNdi standards during analyses gave an average of $^{143}Nd/^{144}Nd=0.511367\pm5$ (n=22, 2σ) and $^{143}Nd/^{144}Nd=0.512110\pm3$ (n=8, 2σ) respectively. Mass fractionation on Pb was monitored using the Tl doping and sample-standard bracketing technique. Data are reported relative to published values of NBS 981 (Catanzaro et al., 1968). 17 replicates of the Pb isotope standard NIST981 gave an average of 17.062±0.002 (2σ) and 15.663±0.002 (2σ) and 37.243±0.007 (2σ) for $^{206}Pb/^{204}Pb$, $^{207}Pb/^{204}Pb$ and $^{208}Pb/^{204}Pb$ respectively. The estimated external precision for Pb analyses is ±0.01%, 2σ for $^{206}Pb/^{204}Pb$ and $^{207}Pb/^{204}Pb$ and ±0.02%, 2σ for $^{208}Pb/^{204}Pb$. Analytical blanks were lower than 40 pg for Nd and 30 pg for Pb.

Text S2.

We selected MORB glass analysis from PetDB [*Lehnert et al.*, 2000], downloaded in November 2014, for the Mid-Atlantic Ridge (MAR), the East Pacific Rise (EPR), the Mid-Cayman Rise and Gakkel Ridge. For Gakkel Ridge, the PetDB data are completed by the dataset from *Gale et al.* [2014]. We filtered marginal compositions for the MORB samples as following: 48.5wt%<SiO_2<60wt%; CaO>9wt%; K_2O<0.4wt%; 5wt%<MgO<10.5wt%.

Table S1. Major (wt%), trace (ppm) and isotopic compositions of the ultramafic and volcanic seafloor basalts (Southwest Indian Ridge).

Table S2. Lithologies, degree of alteration and deformation in all the plagioclase-bearing ultramafic to gabbroic rock samples from the 61° to 67°E region of the SWIR, examined in this study.

Table S3. Major element compositions (wt%) of plagioclases of plagioclase-bearing ultramafic rocks. Average composition of several plagioclase grains in each sample. Error bars: ±1 std.

Table S4. Major element compositions (wt%) of clinopyroxenes of plagioclase-bearing ultramafic rocks. Average composition of several clinopyroxene grains in each sample. Error bars: ±1 std.

Table S5. Major element compositions (wt%) of orthopyroxenes of plagioclase-bearing ultramafic rocks. Average composition of several orthopyroxene grains in each sample. Error bars: ±1 std.

Table S6. Major element compositions (wt%) of olivines of plagioclase-bearing ultramafic rocks. Average composition of several olivine grains in each sample. Error bars: ±1 std.

Table S7. Major element compositions (wt%) of spinels of plagioclase-bearing ultramafic rocks. Average composition of several spinel grains in each sample. Error bars: ±1 std.

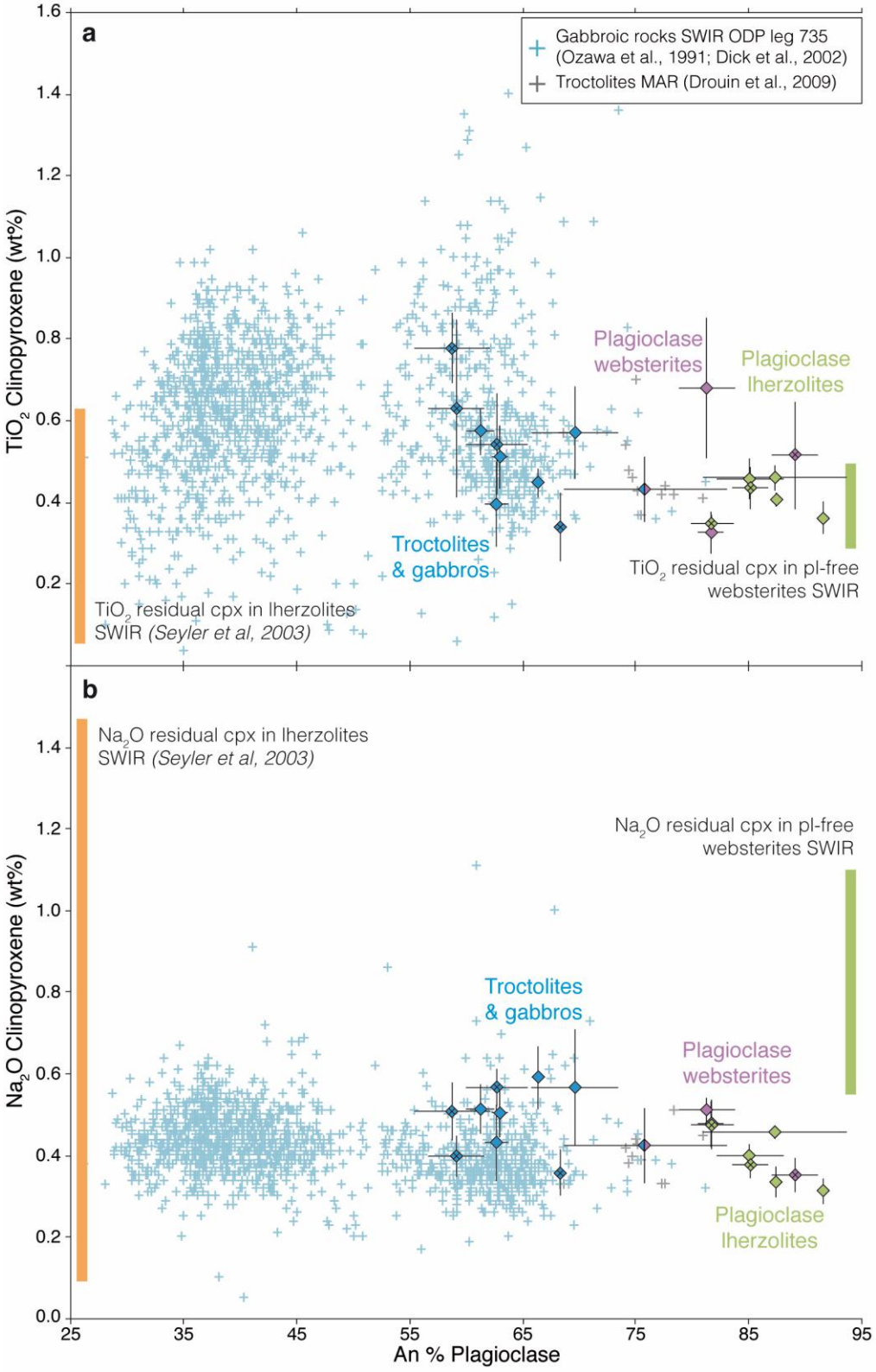

144

145 **Figure S1.** Clinopyroxene and plagioclase major element compositions in samples of the
146 plagioclase-bearing ultramafic to gabbroic suite. (a) Clinopyroxene TiO_2 as a function of

plagioclase anorthite content. (b) Clinopyroxene Na_2O content as a function of plagioclase anorthite content. Diamond data point corresponds to the average composition of several grains in each sample (n values in Tables 5, 6, S3 and S4). Error bars: ±1 std. Diamonds are colored according to modal mineralogy: plagioclase-bearing lherzolites in green, plagioclase-bearing websterites in purple, troctolites, olivine gabbros and gabbros in blue. The blue-purple diamond corresponds to hybrid sample SMS6-5-7 described in Figure 9b. Diamonds with a cross inside correspond to samples for which we also analyzed in-situ trace elements. Orange and green bars show ranges of composition reported for residual clinopyroxenes in plagioclase-free peridotite samples [*Seyler et al.*, 2003] and in plagioclase-free websterites [Brunelli et al., unpublished data] respectively.

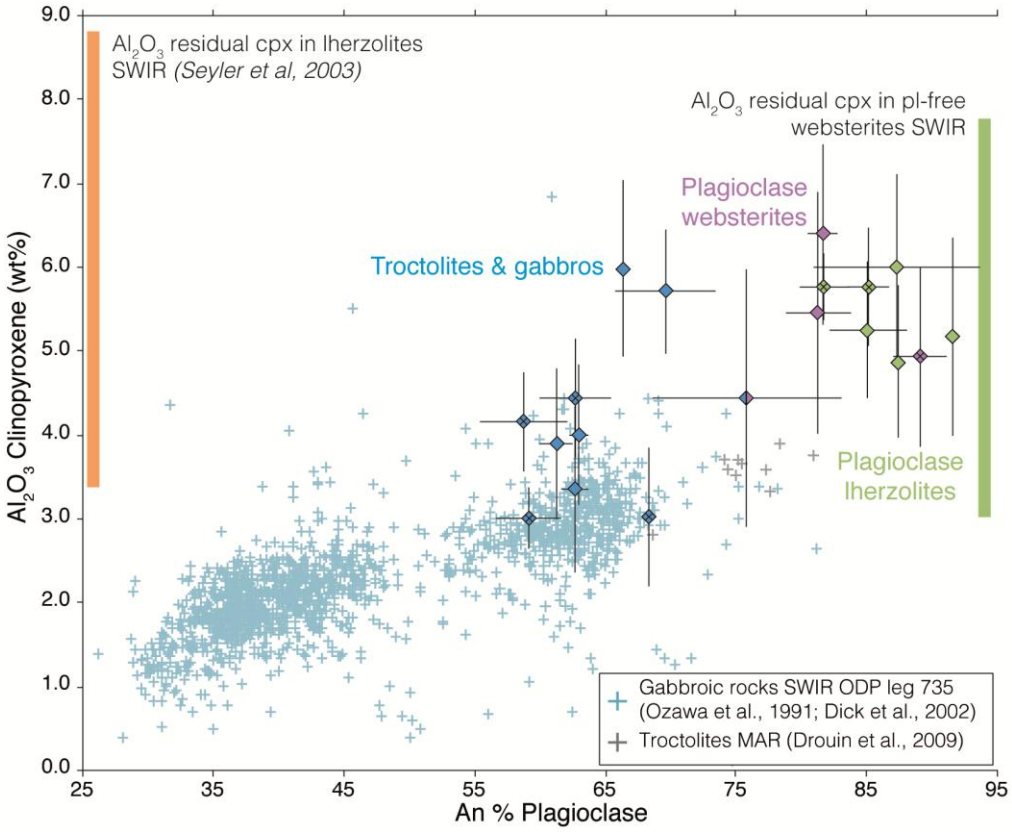

Figure S2. Clinopyroxene and plagioclase major element compositions in samples of the plagioclase-bearing ultramafic to gabbroic suite. Clinopyroxene Al_2O_3 as a function of plagioclase anorthite content. Diamond data point corresponds to the average composition of several grains in each sample (n values in Tables 5, 6, S3 and S4). Error bars: ±1 std. Diamonds are colored according to modal mineralogy: plagioclase-bearing lherzolites in green, plagioclase-bearing websterites in purple, troctolites, olivine gabbros and gabbros in blue. The blue-purple diamond corresponds to hybrid sample SMS6-5-7 described in Figure 9b. Diamonds with a cross inside correspond to samples for which we also analyzed in-situ trace elements. Orange and green bars show ranges of composition reported for residual clinopyroxenes in plagioclase-free peridotite samples [*Seyler et al.*, 2003] and in plagioclase-free websterites [Brunelli et al., unpublished data] respectively.

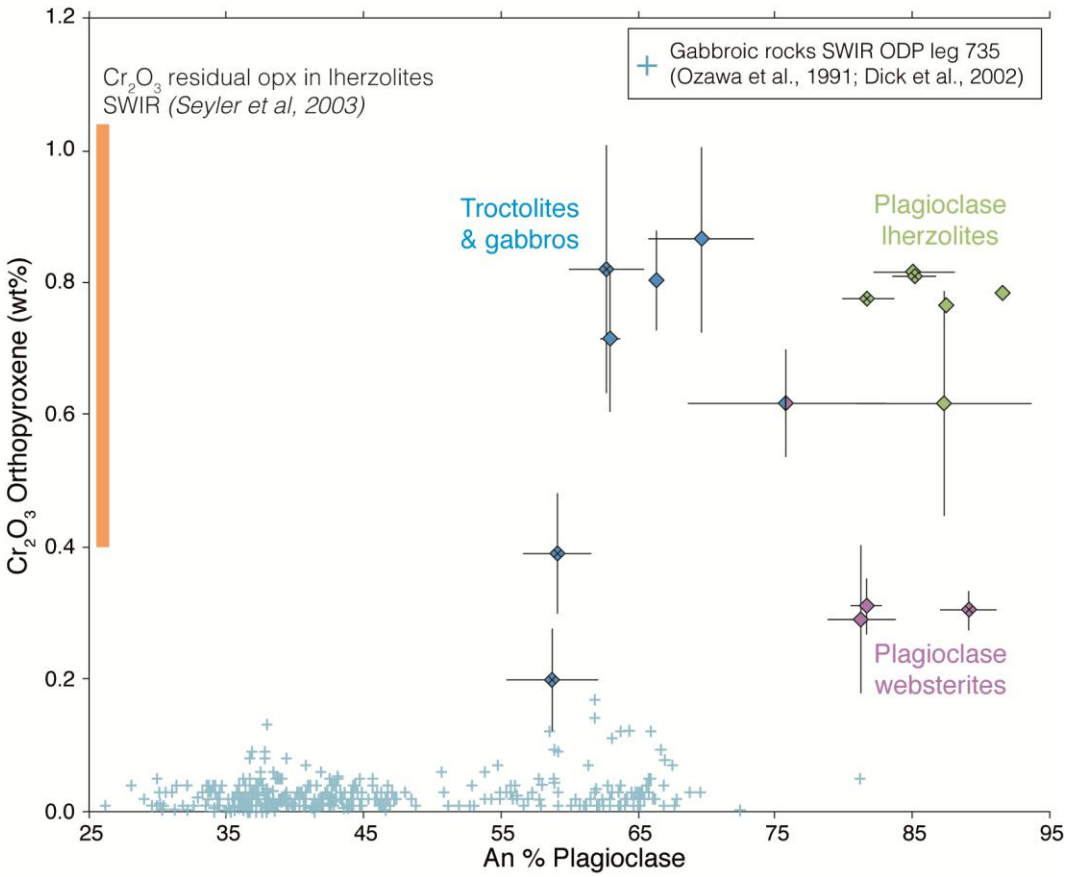

Figure S3. Orthopyroxene and plagioclase major element compositions in samples of the plagioclase-bearing ultramafic to gabbroic suite. Orthopyroxene Cr_2O_3 content as a function of plagioclase anorthite content. Diamond data point corresponds to the average composition of several grains in each sample (n values in Tables 7 and S5). Error bars: ±1 std. Diamonds are colored according to modal mineralogy: plagioclase-bearing lherzolites in green, plagioclase-bearing websterites in purple, troctolites, olivine gabbros and gabbros in blue. The blue-purple diamond corresponds to hybrid sample SMS6-5-7 described in Figure 9b. Diamonds with a cross inside correspond to samples for which we also analyzed in-situ trace elements. Orange bar shows the range of composition reported for residual orthopyroxenes in plagioclase-free peridotite samples [*Seyler et al.*, 2003].

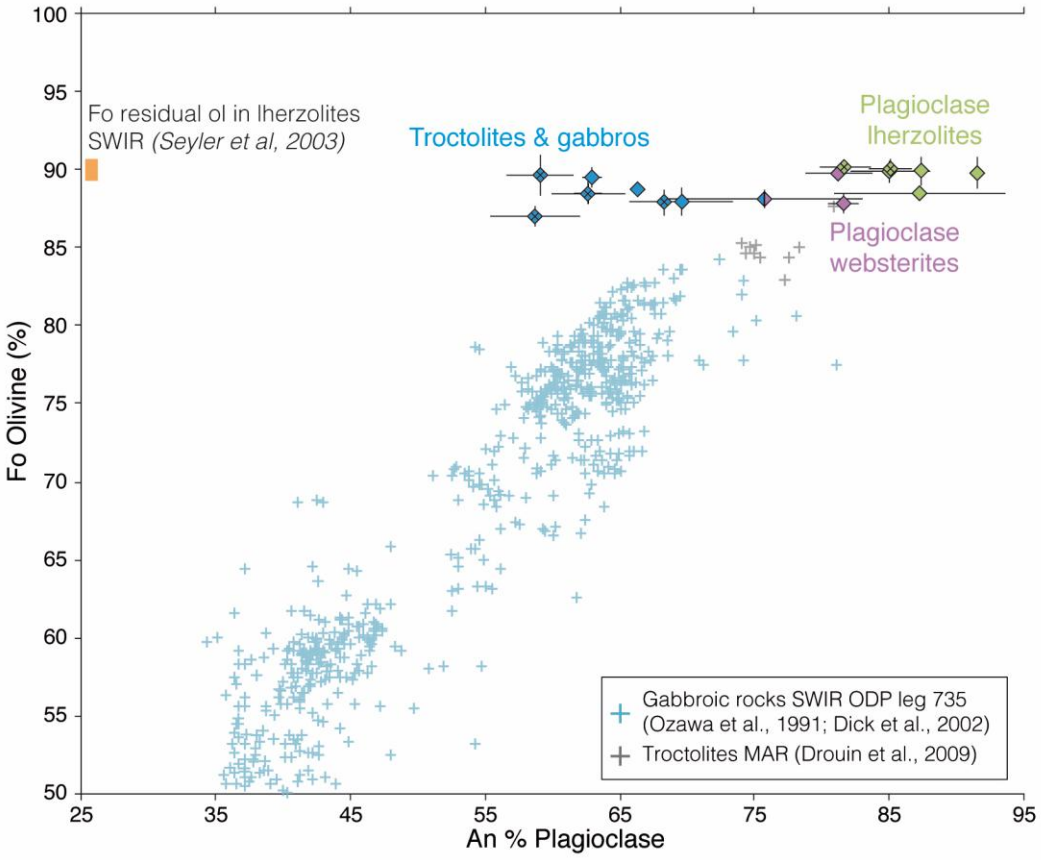

Figure S4. Olivine and plagioclase major element compositions in samples of the plagioclase-bearing ultramafic to gabbroic suite. Olivine Fo content as a function of plagioclase anorthite content. Diamond data point corresponds to the average composition of several grains in each sample (n values in Tables 8 and S6). Error bars: ±1 std. Diamonds are colored according to modal mineralogy: plagioclase-bearing lherzolites in green, plagioclase-bearing websterites in purple, troctolites, olivine gabbros and gabbros in blue. The blue-purple diamond corresponds to hybrid sample SMS6-5-7 described in Figure 9b. Diamonds with a cross inside correspond to samples for which we also analyzed in-situ trace elements. Orange bar shows the range of composition reported for residual olivines in plagioclase-free peridotite samples [*Seyler et al.*, 2003].

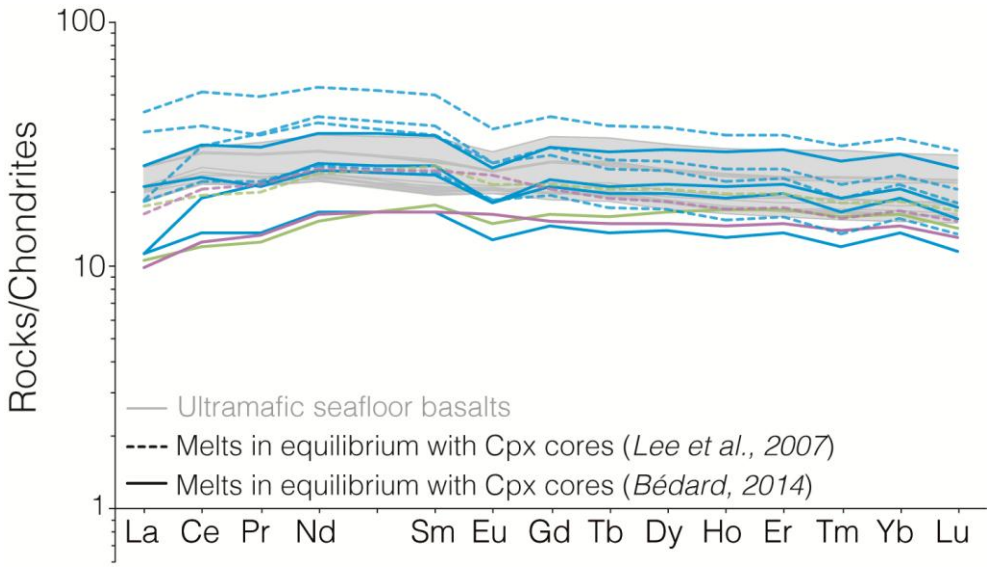

Figure S5. Chondrite-normalized Rare Earth Element (REE) concentrations in melts calculated to be in equilibrium with the clinopyroxenes using clinopyroxene/liquid partition coefficients from *Bédard* [2014] (solid lines) and *Lee et al.* [2007] (dashed lines). Normalizing values of *McDonough and Sun* [1995]. Data are colored according to modal mineralogy of the sample: plagioclase-bearing lherzolites in green, plagioclase-bearing websterites in purple, troctolites, olivine gabbros and gabbros in blue. The field of ultramafic seafloor basalts (Figure 4a) is shown for comparison.

Text S3.

In this model, two parameters are unknown: the parent melt composition of the erupted melt, and the melt-mantle ratio of the reaction, which corresponds to the mass of extracted liquid after the reaction over the initial mass of ultramafic reacted rock. We calculate the composition of the parent melt of the ultramafic seafloor basalt for different values of a melt-mantle ratio (30, 50, 100 and 500), with either no solid mass change, or with a solid mass change of 100%.

For example, taking the ultramafic seafloor basalt SMS16-3-5 as the reacted melt, the olivine gabbro SMS17-5-6 as the reacted solid, and the residual spinel lherzolite ED21-5-1 as the reacting solid, we used the following mass balance equation to calculate the composition of the parent melt:

$$C^i_{parentmelt} = (C^i_{SMS17-5-6} * S_1 + C^i_{SMS16-3-5} * L_1 - C^i_{ED21-5-1} * S_0)/L_0$$

where $C^i_{parentmelt}$ and $C^i_{SMS16-3-5}$ correspond to the concentration of the element i in the parent melt and the erupted ultramafic seafloor basalt SMS16-3-5, respectively. $C^i_{SMS17-5-6}$ and $C^i_{ED21-5-1}$ correspond to the bulk concentration of the element i, respectively in the reacted solid SMS17-5-6 and the reacting solid ED21-5-1, and calculated with modal abundances and the concentrations of the element i in the mineral phases (olivine, orthopyroxene, clinopyroxene, spinel and plagioclase). S_0 and L_0 represent the mass of residual

solid and parent melt respectively, whereas S_1 and L_1 represent the mass of reacted solid and liquid (SMS17-5-6 and SMS16-3-5) respectively.

We define $S_1 = S_0 + dS$, where dS is the change of solid mass after reaction. In our calculations, $dS = y * S_0$, where y is the ratio of change of solid mass after reaction. If all the olivine is residual, y varies between 0 and the ratio of the modal abundances of olivine in the residual peridotite and in the reacted solid. If dS=0, the mass of initial peridotite corresponds to the same mass of reacted solid; if there is significant modal plagioclase in the reacted solid, this implies that there has been melt trapping and that the reaction zone has grown in volume. If the reaction is mostly clinopyroxene replacing orthopyroxene, it could be nearly isovolume. Note that the calculation as it is done does not take into account the possibility of a net decrease in solid mass resulting from the melt/mantle reaction.

The mass of reacted liquid is given by $L_1 = R * S_0$, where R is the melt/mantle ratio, and the mass of parent melt is given by $L_0 = dS+L_1$.

The model is most sensitive to the choice of reacted solid composition. We made the assumption that the most representative composition was that of SMS17-5-6, an olivine gabbro. If we had a more extensively reacted composition (such as ED21-10-3), the calculated melt/rock ratios needed to go from parent to reacted melts of a given composition would be larger.

Table S8. Major (wt%) and trace (ppm) compositions of the ultramafic seafloor basalt SMS16-3-5, and of plagioclase-bearing and plagioclase-free ultramafic rocks. Compositions for SMS17-5-6 and ED21-5-1 correspond to reconstructed bulk composition using modal abundances from Table 4, and *Seyler et al.* [2011], respectively.

	SMS16-3-5	SMS23-2-10	SMS17-5-6	ED21-5-1
SiO_2	50.42	50.37	46.96	44.53
TiO_2	1.34	1.34	0.20	0.05
Al_2O_3	17.24	16.83	14.85	2.36
FeO	7.59	8.01	4.27	8.22
MnO	0.14	0.14	0.07	0.16
MgO	8.64	8.25	16.79	43.45
CaO	9.76	10.20	12.05	1.37
Na_2O	4.16	3.76	1.70	0.04
K_2O	0.18	0.19	0.01	0.00
Cr_2O_3	0.05	0.05	0.85	0.41
Sc	29.10	32.40	21.09	5.18
Sr	220.34	174.91	21.08	2.83
Zr	101.53	100.97	1.20	0.39
La	4.82	4.43	0.51	0.00
Ce	14.83	13.33	0.93	0.01
Nd	10.33	10.37	2.05	0.05
Sm	2.89	3.14	2.81	0.05
Eu	1.11	1.14	4.03	0.02
Gd	3.68	4.22	3.09	0.10
Dy	4.20	4.84	3.21	0.17
Er	2.53	3.02	3.14	0.14
Yb	2.43	2.96	2.97	0.17
Lu	0.37	0.44	2.51	0.03
Y	37.73	25.06	2.74	1.10

Text S4.

During the calculations presented Figures 13 and 15, pressure is kept constant, and each step corresponds to 0.01% of extraction. We used Danyushevsky model from 2001 for olivine, plagioclase and clinopyroxene fractionation. The oxygen fugacity is calculated following Borisov and Shapkin model [1990]; melt density is calculated following the model of Lange and Carmichael [1987]; melt viscosity is calculated following the model of Bottinga and Weill [1972]. Before the beginning of the calculations, Petrolog recalculates the composition of the basalt, Fe_2O_3 content being calculated using QFM-1 buffer for oxygen fugacity. This explains why the starting composition plotted Figure 13 does not fit exactly the SMS16-3-5 composition.

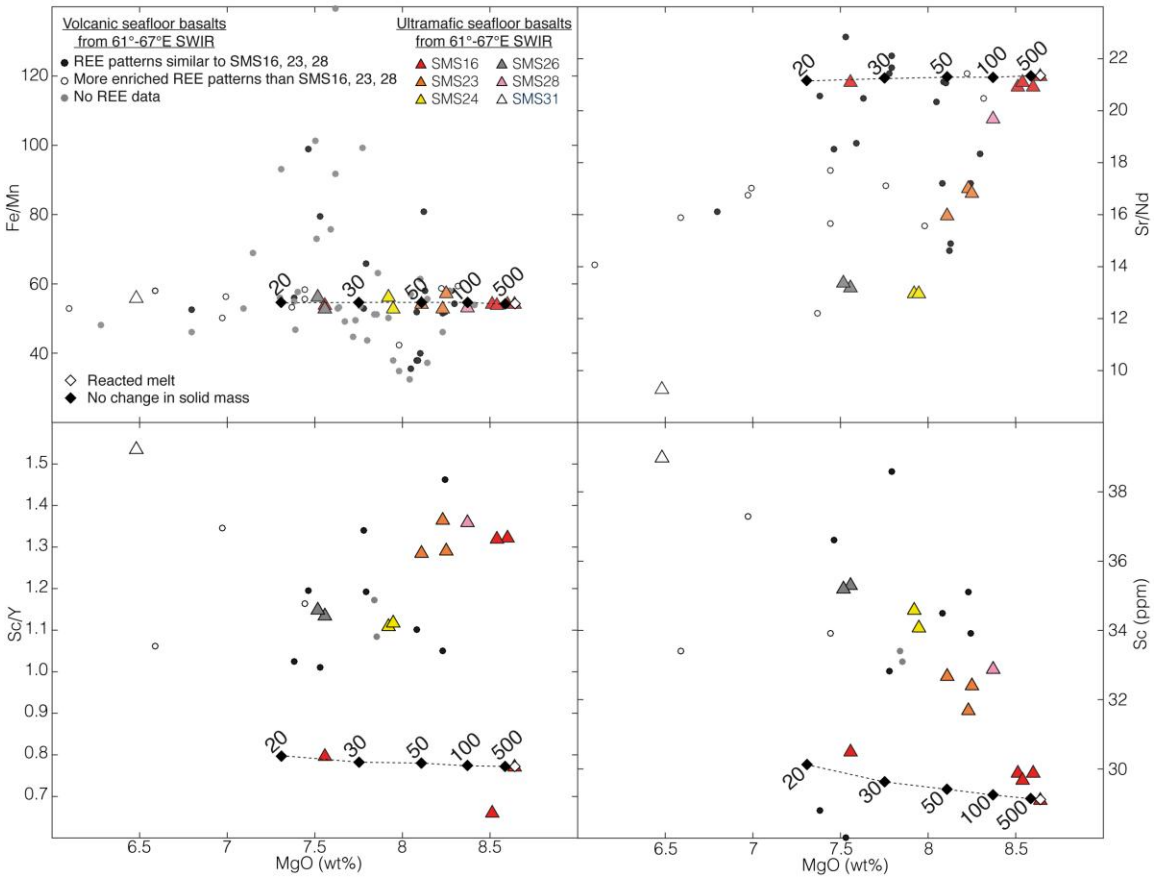

Figure S6. Mass balance model of the possible effect of melt-rock interactions in the mantle lithosphere on the major element composition of basalts in the easternmost Southwest Indian Ridge. See caption of Figure 13 for the details. (**a**) Fe/Mn, (**b**) Sr/Nd, (**c**) Sc/Y and (**d**) Sc content in function of MgO content.